buildings

MDPI

Article

Chloride Ion Corrosion Resistance of Innovative Self-Healing SMA Fiber-Reinforced Engineering Cementitious Composites under Dry-Wet Cycles for Ocean Structures

Weihong Chen [1], Yi Liu [1], Hui Qian [2,*], Peng Wu [2], Yingxiong Wu [1] and Fanghao Liu [1]

[1] College of Civil Engineering, Fuzhou University, Fuzhou 350116, China
[2] School of Civil Engineering, Zhengzhou University, Zhengzhou 450001, China
* Correspondence: qianhui@zzu.edu.cn

Abstract: To evaluate the chloride ion corrosion resistance of proposed innovative self-healing concrete based on shape memory alloys (SMA) and engineering cementitious composites (ECC), a total of 2 kinds of 22 specimens were prepared. Chloride ion corrosion tests of self-healing SMA-ECC concrete under dry-wet cycles were carried out. It was found that the chloride ion erosion depths of SMA-ECC were significantly smaller than that of MC, and the growth rate of erosion depth of SMA-ECC was obviously smaller than that of MC after 15 dry-wet (dry and wet) corrosion cycles. The chloride ion content of SMA-ECC vanished at the erosion depth more than 10 mm, which was consistent with the test result of $AgNO_3$ solution color-rendering test. Test results indicate that, compared to marine concrete (MC), SMA-ECC has a better chloride ion corrosion resistance behavior. Moreover, the chloride ion concentration of SMA-ECC at a chloride ion erosion depth of less than 10 mm decreased more significantly than that of MC, indicating that almost all chloride salt solution reacted in the outer layer of SMA-ECC, which is consistent with the conclusions of 4.1 and 4.2. Finally, based on the erosion distribution of chloride ions and Fick's second law, a calculation model describing the relationship between the apparent chloride ion diffusion coefficient and the boundary condition of the chloride ion content was proposed.

Keywords: self-healing; dry-wet cycles; chloride ion corrosion resistance; non-destructive; marine concrete

check for updates

Citation: Chen, W.; Liu, Y.; Qian, H.; Wu, P.; Wu, Y.; Liu, F. Chloride Ion Corrosion Resistance of Innovative Self-Healing SMA Fiber-Reinforced Engineering Cementitious Composites under Dry-Wet Cycles for Ocean Structures. *Buildings* **2023**, *13*, 518. https://doi.org/10.3390/buildings13020518

Academic Editor: Elena Ferretti

Received: 9 November 2022
Revised: 27 December 2022
Accepted: 7 January 2023
Published: 14 February 2023

Copyright: © 2023 by the authors. Licensee MDPI, Basel, Switzerland. This article is an open access article distributed under the terms and conditions of the Creative Commons Attribution (CC BY) license (https://creativecommons.org/licenses/by/4.0/).

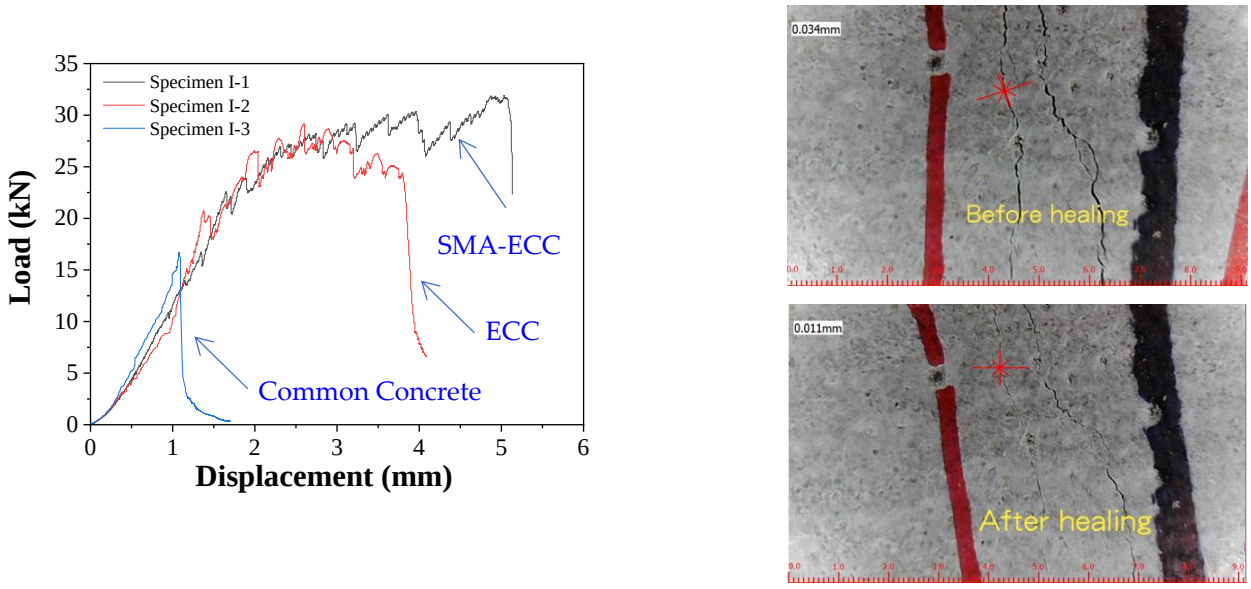
1. Introduction

Concrete members generally undergo load and environment changes with cracks in the service-level stage. Concrete cracks provide a convenient path for the penetration of chloride ion, resulting in accelerating the corrosion of steel bars, consequently affecting the durability of the structure and causing huge economic loss [1]. Marine environments are very aggressive to concrete structures, and especially dry-wet cycle condition promotes the transmission of chloride ions in concrete, always identified as the most unfavorable environment condition for concrete deterioration processes [2,3].

Many researches show that it is an effective strategy to form a film on the concrete surface to protect concrete from corrosion [4]. There are several methods for preventing or delaying the penetration of chloride ion and the corrosion of steel bars in concrete, such as organic inhibitors and coatings [5–7]. A kind of silica-based hybrid nanocomposite was used for surface treatment of hardened cement-based materials, and this kind of material can significantly decrease water absorption rate and gas permeability coefficient [8]. Soluble sodium silicate as a surface treatment material could obviously improve the impermeability because soluble sodium silicate can react with portlandite and form C-S-H gel, which can refine the pore structure and densify the surface structure [9]. Cementitious composites prepared with different types of fly ash can also improve the resistance to chloride ion penetration of concrete [10]. Electrochemical methods leading to chloride extraction or

cathodic protection have also been used to protect reinforced concrete structures [11,12]. However, the above measures can only reduce the permeability but cannot inhibit the development of cracks. In the long run, the problem of anti-chloride corrosion has not been fundamentally solved.

Shape memory alloy (SMA) is a type of intelligent material that "remembers" its original shape. Two major properties of SMA, the shape memory effect and super-elasticity, could be used for self-rehabilitation of concrete structures [13]. Engineered cementitious composite (ECC) [14] is a new type of fiber reinforced cementitious composite (FRCC) with extremely high tensile strain capacity of 3% or more, which provides favorable conditions for crack self-control and self-healing of small cracks and has the characteristics of multi-micro cracking. Based on the characteristics of SMA fiber's superelasticity and ECC's multi-micro cracks, Chen et al. [15] developed a smart self-healing composite material SMA-ECC in which shape memory alloy fibers were added into the engineered cementitious composite material to achieve good self-healing properties and better prevent the migration of chloride ions. The uni-axial tensile test was carried out on the SMA-ECC specimen. The stress-strain curves of SMA-ECC specimen under uni-axial tension are shown in Figure 1a. The SMA-ECC material can undergo large deformation under relative higher bearing loading. Moreover, the self-healing performance of the innovative material were experimentally studied. The influence of pre-loading level and SMA content on the self-healing behavior were considered. It was found that the bending strength and deflection of SMA-ECC increased with the increase of SMA fiber content, the cracks with width less than 50 μm were almost completely closed, and the cracks with a width of over 100 μm were able to recover 67% [16]. The contrast figures before and after recovery of cracks are shown in Figure 1b.



(**a**) (**b**)

Figure 1. The stress-strain curves and crack comparison of SMA-ECC. (**a**) The stress -strain curves of SMA-ECC specimen under uni-axial tension [13]. (**b**) Cracks comparison of SMA-ECC beam before and after self-healing [14].

When the self-healing material is exposed to chloride solution, a chloride concentration gradient will occur between the surface of the self-healing material and the pore solution. In this case, diffusion will be the main driving mechanism of chloride transport. Since SMA fiber is not an economical material, considering that its mixture with mortar or ECC can be applied to the protective layer in marine concrete structures, it is necessary to research the chloride ion corrosion resistance of SMA-ECC, both its non-destructive state and cracked

state were studied. This paper only showed that the chloride ion corrosion resistance of self-healing concrete in the non-destructive state under the combined action of chloride ion corrosion and repeated dry-wet cycles, which compared with that of MC.

2. Experimental Program

2.1. Specimen Design

According to the mixing ratio, dry materials, including cement, mineral powder, fly ash and quartz sand, were weighed, and then mixed for more than 1 min to ensure uniform mixing. Then water and water reducer were configured into a mixed solution, and slowly poured into the mixture during the stirring process. When the wet-mixed mixture had a certain fluidity, the polyvinyl alcohol (PVA) fibers and shape memory alloy (SMA) fibers were sprinkled into it, and wet-mixed mixture continued stirring for more than 3 min until the fibers were evenly dispersed. The SMA-ECC mixture was poured into an oil-coated mold, covered with plastic wrap, demolded after 24 h, and standardly cured for 28 days. MC specimens were also prepared for comparison. The mechanical properties of SMA-ECC and MC were measured after 28-day pouring and curing, as shown in Table 1. A total of 2 categories of 22 specimens were prepared.Among them, there were 11 SMA-ECC specimens and an equal number of MC specimens. According to the design of the material mix ratio, the cube specimens with a size of 100 mm × 100 mm × 100 mm were poured.

Table 1. Mechanical properties of material specimen after 28 -days of standard curing.

Material	Compressive Strength (MPa)	Tensile Strength (MPa)	Ultimate Tensile Strain (%)
SMA-ECC	39.8	3.10	3.45
MC	42.5	/	/

2.2. Material

The mix proportions of MC and SMA-ECC specimens are listed in Tables 2 and 3, respectively. In the tables, the cement used is P. O42.5 ordinary silicate cement. The mineral powder used is 1000 mesh S95 slag powder. The particle size of quartz sand used ranged from 100 mesh to 325 mesh (i.e., 150 μm~45 μm). The fly ash used is 5000 mesh super high-quality fly ash with a density of 2.55 g/cm^3. The natural river sand used has a fineness modulus of 2.39 with an apparent density of 2620 kg/m^3 and a bulk density of 1895 kg/m^3. Because the on-site sand is piled up in open air and has a high water content, it needs to be dried before using. The particle size of the gravel used is 5 mm~10 mm continuous gradation, and the apparent density is 2700 kg/m^3. Polyvinyl alcohol (PVA) fiber and shape memory alloy (SMA) fiber were used, and the mechanical properties of the two kinds of fibers are shown in Table 4. PVA fibers and SMA fibers are shown in Figure 2, were used. Polycarboxylate superplasticizer is the water reducer with a water reduction rate of 38%. the dose of the water reducer is typically 0.15 percent to 0.3% of the mass of the entire cementitious material. The water used was ordinary tap water, and the chloride ion content was detected using distilled water.

Table 2. Mix proportion of MC.

Material	Cement	Fly Ash	Gravel	Sand	Water
MC	1.0	0.24	3.26	2.00	0.47

Table 3. Mix proportion of SMA-ECC.

Material	Cement	Mineral Powder	Fly Ash	Sand Binder Ratio	Water-Binder Ratio	PVA Fiber (V%)	SMA Fiber (V%)
SMA-ECC	0.15	0.15	0.70	0.40	0.25	2.00	0.70

Table 4. Mechanical properties of PVA and SMA fiber.

Fiber Type	Diameter (mm)	Length (mm)	Tensile Strength (MPa)	Elongation at Break (%)	Elastic Modulus (GPa)	Density (g/cm^3)
PVA	0.04	12	1560	6.5	42	1.30
SMA	0.6	16	895	38	41	6.45



(**a**) (**b**)

Figure 2. PVA fiber and SMA fiber pictures. (**a**) PVA fiber; (**b**) SMA fiber.

3. Test and Measurement Methods

3.1. Dry-Wet Corrosion Cycle Test

The laitance on the eroding side surface of the cube specimens was first removed after conventional curing for 28 days, and it was then ground off before being placed in a 60 °C incubator to dry for 3 days. The other surfaces were coated with epoxy resin in addition to keeping the pouring surface as the erosion surface to assure the one-dimensional transmission of chloride ion erosion, and the smeared specimen is displayed in Figure 3. Finally, the content of NaCl analytical pure preparation was 5% (mass fraction) of chloride salt solution, as shown in Figure 4. The dry-wet system of the chloride salt dry-wet corrosion cycle test involved immersion in chloride salt solution for 3 days in a natural setting, followed by 1 day of drying at 60 °C and 4 days of dry-wet corrosion. Before drying, it is necessary to ensure that there is no obvious moisture residue on the surface of the specimens. If the specimens were cooled after drying, immersion corrosion can be performed [17,18]. The daily variations in ambient temperature were recorded during the soaking phase.



Figure 3. Specimen coated with epoxy resin.

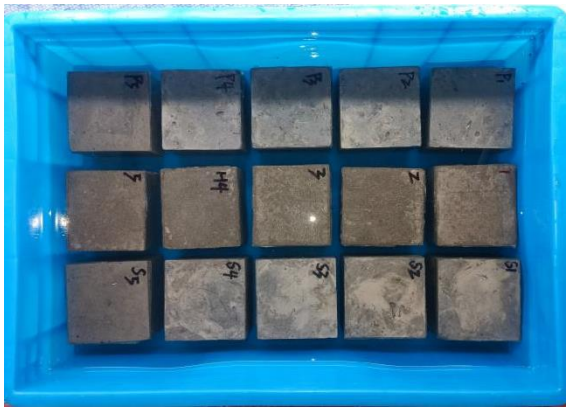


Figure 4. Specimens being soaked.

3.2. Chlorine Salt Solution Transmission Amount Detection

After immersion and drying in each dry-wet corrosion period, the corroded specimens (SMA-ECC and MC) were weighed using an electronic scale with a weighing accuracy of 0.1 g. The erosion of the solution during the soaking stage and the evaporation of the solution during the drying stage were recorded for various times of the dry-wet cycle. In order to ensure the measurement accuracy, the corroded specimens in soaking stage were wiped dry before weighing.

There was a close correlation between the transmission amount of chloride salt solution and the porosity of the specimen. For example, the capillary flowing in soaking stage during the dry-wet corrosion cycle process can accelerate the corrosion of chloride ions on the specimen. For the measurement method of porosity of the specimen, please refer to "GB/T 24586-2009 Determination of apparent density, true density and porosity of iron ore". The calculation Formula (1) is as follows:

$$\phi = (\rho_r - \rho)/\rho_r \quad (1)$$

where ϕ represents the porosity (%); ρ and ρ_r represent the apparent density and true density, respectively. Among them, the apparent density of the specimen can be calculated by Archimedes' law and density formula; the true density is measured by the true density instrument −1340. In addition, before detecting the apparent density ρ and true density ρ_r of the specimen, the specimen needs to be dried in a constant temperature oven at 60 °C. When the mass difference of the specimen for 2 consecutive days is less than 0.1%, the specimen is considered to be completely dry [19]. To ensure the accuracy of the results, the number of the specimens in the same condition should not be less than 3.

3.3. Chloride Ion Erosion Depth Detection

At present, most scholars mainly used a cutting machine to cut the corroded specimen to obtain a section for the chloride ion erosion depth detection method of cement matrix materials, and then conducted a nitrate solution color-rendering test for the chloride ion erosion depth on the section. However, the frictional squeezing of the cutting process leads to powder residues in different positions, resulting in inaccurate color-rendering of the erosion depth. In order to assure the flatness of the split surface, this test first cut the opposite side and both sides of the eroded surface of the specimen to make a groove, as shown in Figure 5. A self-made splitting device was used to split the corroded specimen, as shown in Figure 6.



Figure 5. Pretreatment of split specimen.

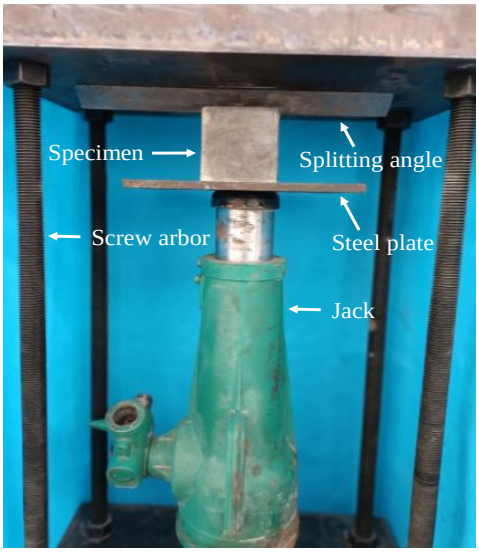
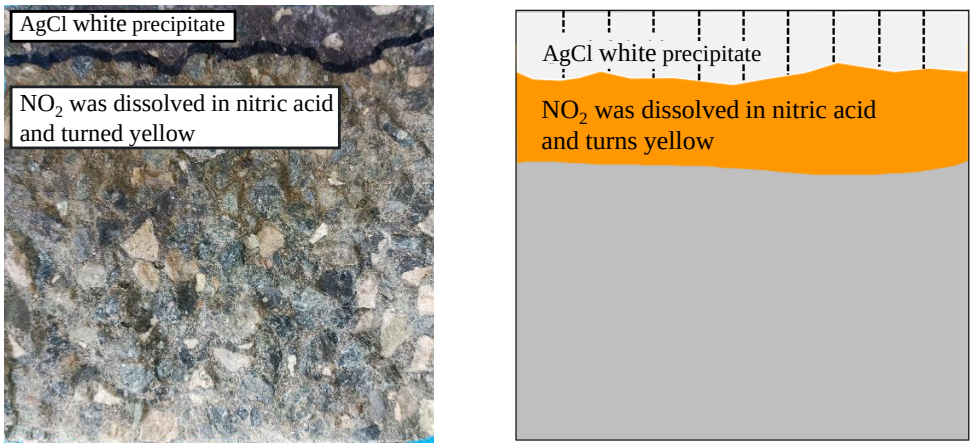


Figure 6. On-site splitting of corroded specimen.

The $AgNO_3$ solution with a content of 0.1 mol/L was sprayed on the split surface of the specimen to observe the corrosion depth of chloride ions. After about 15 min, white AgCl precipitates formed in the area eroded by chloride salt, and the $AgNO_3$ solution in the uneroded area was decomposed by light to produce NO_2, which was dissolved in nitric acid and turned yellow. According to the area of the observed color change, a waterproof pen was used to trace the erosion outline at the border of white and yellow, as shown in Figure 7a. The eroded surface of the specimen was divided into 10 equal parts in the direction perpendicular, as shown in Figure 7b. Finally, considering the uneven section of the pressure-splitting specimen, the depth of the chloride ion erosion was determined by measuring the distance between the specimen's color-rendering boundary and erosion surface using a vernier caliper and a level ruler. This measurement was accurate to 0.1 mm.

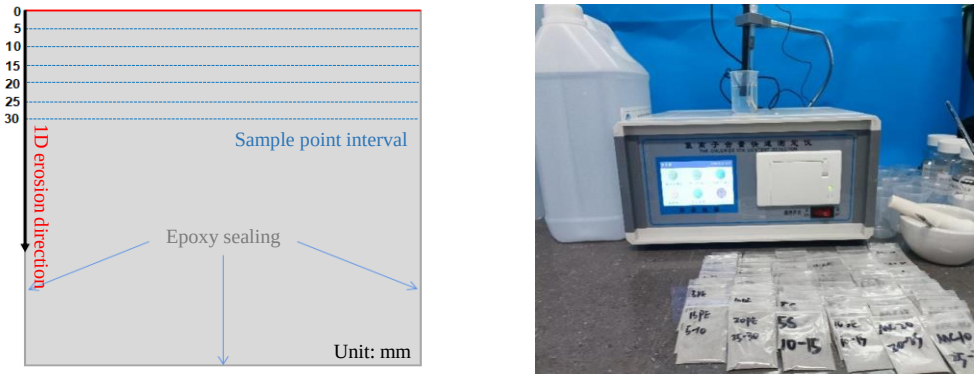


(**a**) (**b**)

Figure 7. $AgNO_3$ solution color-rendering test. (**a**). Split surface of corroded specimen. (**b**). Schematic diagram of an equally divided splitting plane.

3.4. Chloride Ion Content Detection

First, on the split surface along the erosion depth direction, multi-point sampling (impact drill or pulverizer) was carried out at intervals of 5 mm depth until 30 mm. The specimen of the mesh sieve was placed in a 60 ± 5 °C incubator and dried for 2 days. Finally, 2 g of the specimen was cooled to 20 °C and configured with distilled water as a solution of 40 mL, and a chloride ion content detection was used to measure chlorine ion content after standing for 1 day, as shown in Figure 8. The test results were taken as the average of the content of three specimens.



(**a**) (**b**)

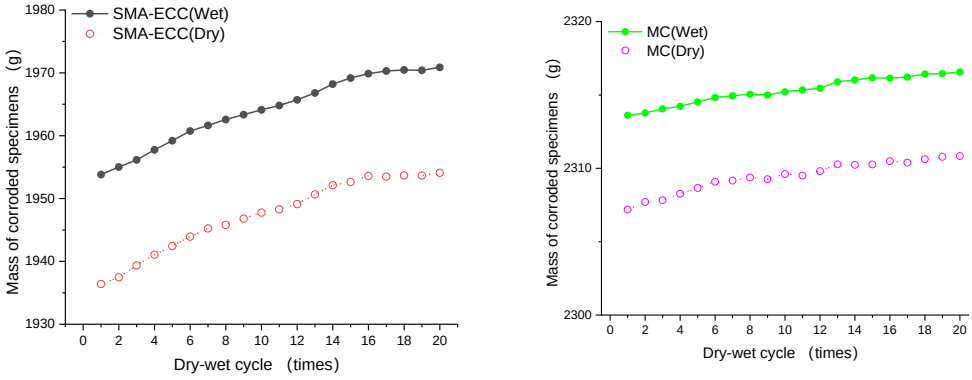
Figure 8. Chloride ion content detection. (**a**) Schematic diagram of split section (**b**) Chloride ion content detection.

4. Test Results

4.1. Mass Change of Specimen during Corrosion

The specimen was corroded by a chloride salt solution, and physical and chemical reactions took place at the surface of the corroded specimen in contact with the solution. For example, unhydrated cement particles reacted by hydrating, mineral admixtures reacted by secondary hydrating, and chloride ions combined, causing the specimen's surface pores to be densely filled [20–24]. If transport behavior of the chloride salt solution is changed, the corrosion behavior of chloride ions will be affected. The transmission characteristics of the chloride salt solution were analyzed with the increase in dry-wet cycle times by recording the mass of the specimens after immersion and drying under the process, and further calculating the capillary absorption and diffusion evaporation of the corrosion solution under each stage, which served as a reference for the subsequent variation rule of

chloride ion erosion. By weighing the corroded specimens after drying and immersion in each chloride salt dry-wet corrosion cycle process, with the increase of times of dry-wet cycle, the average mass of the SMA-ECC and MC specimens under chloride salt dry-wet corrosion cycle changed, as shown in Figure 9.



(**a**) (**b**)

Figure 9. Mass change of corroded specimens under dry-wet cycles. (**a**) SMA-ECC (**b**) MC.

As shown in Figure 9, the mass of the specimens of SMA-ECC and MC almost continuously increased in the whole process. For example, after 20 times of chloride salt dry-wet corrosion cycle, the mass changes of SMA-ECC and MC in drying stage were +17.70 g and +3.65 g, respectively, and the mass changes in soaking stage were +17.06 g and +2.95 g. This occurred because, as the specimens were being affected by the chloride salt solution, external substances such water, sodium chloride, and carbon dioxide underwent physical adsorption and chemical fusion with the material, increasing the bulk of the corroded specimens.

During corrosion process, the mass changes of SMA-ECC specimens mainly occurred in the first 15 dry-wet cycles, and there was almost no obvious change in the mass of the specimens after 15 dry-wet cycles. After 20 times of chloride salt dry-wet corrosion cycle, the mass increase of SMA-ECC in drying stage was about 4.8 times that of MC, and the mass increase of SMA-ECC in soaking stage was about 5.8 times that of MC, which indicated that compared with MC, SMA-ECC underwent more severe physical and chemical reactions at the erosion surface of the specimens during corrosion process.

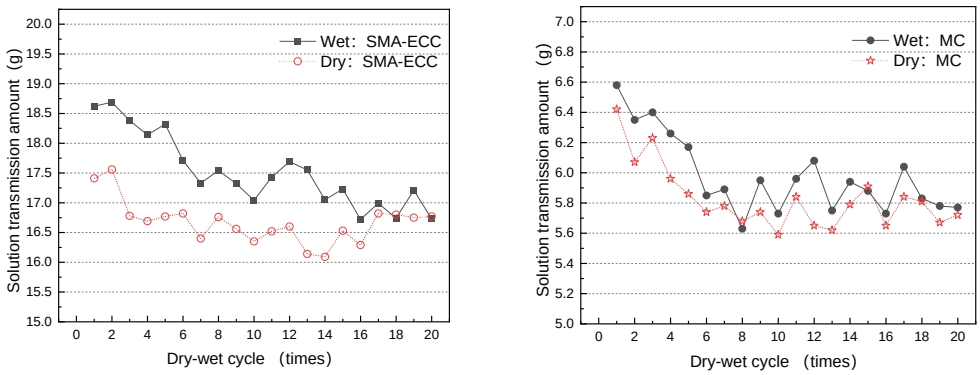
4.2. Change Law of the Transmission Amount of Chloride Salt Solution

During dry-wet cycle, the chloride salt solution acted as corrosion carrier of chloride ion, and its transport behavior played a key role in the corrosion of chloride ion [25]. The transmission of chloride salt solution in dry-wet corrosion cycle was mainly divided into capillary absorption of liquid solution in soaking stage and diffusion evaporation of gaseous solution in drying stage. The erosion amount of the solution and calculation formula of that is shown in Formula (2); by comparing the quality of the immersed and dried corroded specimens in each dry-wet stage, the evaporation of the gaseous chloride salt solution was calculated, and the calculation formula is shown in Formula (3). The transmission amount changes of liquid and gaseous chloride salt solutions of SMA-ECC and MC specimens under the action of chloride salt dry-wet corrosion cycle are shown in Figure 10.

$$\Delta m_{lw} = m_w^{i+1} - m_d^i \quad (2)$$

$$\Delta m_{gw} = m_w - m_d \quad (3)$$

where Δm_{gw} represents the evaporation of gaseous chloride salt solution (g); Δm_{lw} represents the absorption of liquid chloride salt solution (g); m_w and m_d represent the mass (g) of the corroded specimen after soaking and drying during each dry-wet corrosion cycle, respectively.



(**a**) (**b**)

Figure 10. Transport behavior of chloride salt solution of specimens under different times of dry-wet corrosion cycle. (**a**) SMA-ECC (**b**) MC.

As shown in Figure 10, with the increase of the times of dry-wet corrosion cycle, the capillary absorption of the external chloride solution in soaking stage and the evaporation of pore chloride salt solution in drying stage of SMA-ECC and MC specimens during each dry-wet corrosion cycle all showed a trend of first decreasing and then stable fluctuation. For example, when the times of dry-wet corrosion cycle increased from 0 to 5, the capillary absorption of the chloride salt solution of SMA-ECC specimen in soaking stage decreased from 18.69 g to 18.14 g, and the evaporation of the pore solution in drying stage decreased from 17.56 g dropped to16.77 g; at the late period of the corrosion process, that is, after 15 dry-wet cycles, the transmission amount of chloride salt solution in soaking stage and drying stage fluctuated around 16.5 g (±0.5 g).

Comparing the transmission amount of chloride salt solution of SMA-ECC and MC specimens in each dry-wet corrosion stage, it was found that the solution transmission amount of SMA-ECC was significantly greater than that of MC, whether it was the evaporation amount of the solution in drying stage or the erosion amount of the solution in soaking stage.Based on the analysis and conclusion of Mass change of specimen during corrosion, compared with MC, due to the more violent chemical and physical reaction of SMA-ECC in the eroded outer layer, the reaction products of the outer layer of SMA-ECC caused expansion and microcracks, which eventually led to the increase of porosity of its outer layer, that is, the permeability became worse.

4.3. Change Law of Corrosion Depth of Chloride Ion

The chloride ion corrosion resistance of specimen is closely related to corrosion depth and corrosion content of chloride ion. The corrosion depth of chloride ion exceeds the thickness of the protective layer of concrete and reaches the surface of steel bar, which is very likely to cause corrosion and expansion of steel bar and peeling of the protective layer [26,27]. The $AgNO_3$ solution was used to visualize the corroded specimens of SMA-ECC and MC under 0, 5, 10, 15 and 20 dry-wet cycles during corrosion process. The variation rule of chloride ion erosion depth under different times of dry-wet corrosion cycle is shown in Figure 11.

As shown in Figure 11, the increase of chloride ion erosion depth of SMA-ECC and MC gradually slowed down with the increase times of dry-wet corrosion cycle. Among them, with the times of dry-wet corrosion cycle increased from 0 to 5, 5 to 10, 10 to 15, and 15 to 20, the chloride ion erosion depth of SMA-ECC increased by 5.58 mm, 2.05 mm, 1.08 mm and 0.41 mm, respectively, while that of MC increased by 8.72 mm, 3.49 mm, 2.13 mm and 1.48 mm, respectively. In addition, the chloride ion erosion depth of SMA-ECC never exceed 10 mm during corrosion process. The actual chloride ion erosion depths of two kinds of specimen after dry-wet corrosion cycle are shown in Figure 12. It was found that the chloride ion erosion depths of SMA-ECC were significantly smaller than that of MC, and the growth rate of erosion depth of SMA-ECC was obviously smaller than that of MC

after 5 dry-wet corrosion cycles. The erosion depths of SMA-ECC gradually flattened and stayed at 10 mm after 20 dry-wet corrosion cycles, which was consistent with the test result of $AgNO_3$ solution color-rendering test.

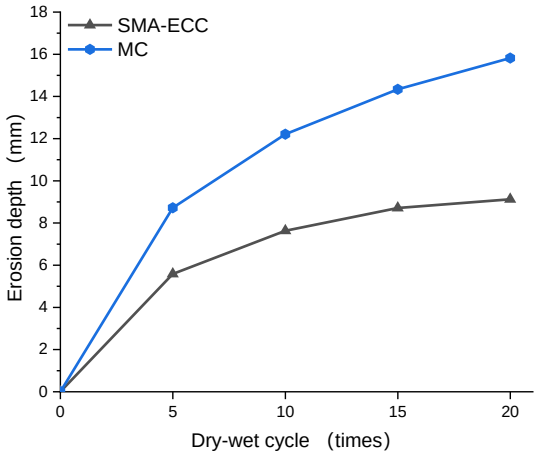


Figure 11. Change law of chloride ion erosion depth of corroded specimens.



(**a**) (**b**)

Figure 12. Erosive Chloride Ion image showing depth of specimen after 20 cycles of dry-wet corrosion. (**a**) SMA-ECC (**b**) MC.

From data mentioned above in the chloride ion erosion depth of SMA-ECC and MC under different times of dry-wet cycle, it can be concluded that: (1) The chloride ion depth corrosion efficiency of SMA-ECC in the first 5 dry-wet cycles accounted for 61.2% of corrosion process, which indicated that the chloride ion corrosion of SMA-ECC mainly occurs in the early stage of corrosion; (2) During dry-wet corrosion cycle, the increase of chloride ion erosion depth of MC specimens under the same times of dry-wet cycle was obviously larger than that of SMA-ECC; (3) After 15 times of dry-wet corrosion cycle, the increase of chloride ion erosion depth of SMA-ECC specimens under the same times of dry-wet cycle became more moderate than that of MC.

4.4. Change Law of Corrosion Content of Chloride Ion

The corrosion content of chloride ion at different erosion depths was detected on the specimens under 0, 5, 10, 15 and 20 times of dry-wet cycle during the corrosion process by using a chloride ion content detection. Considering that the matrix material, the transmission amount of chloride salt solution and the chloride ion erosion depths of SMA-ECC and ECC were basically the same, only the chloride ion content of SMA-ECC and MC specimens at different erosion depths was tested, the test results are shown in Figure 13.

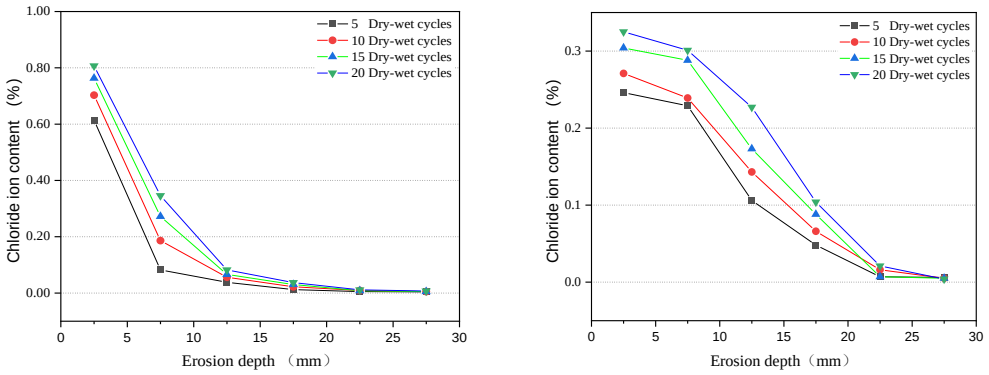


Figure 13. Chloride ion erosion distribution of SMA-ECC and MC specimens. (**a**) SMA-ECC (**b**) MC.

As shown in Figure 13, the chloride ion content of SMA-ECC and MC specimens under dry-wet corrosion cycle were all generally on a downward trend with the increase of the erosion depth. Compared with MC, the chloride ion concentration of SMA-ECC at a chloride ion erosion depth of less than 10 mm decreased very significantly, indicating that almost all chloride salt solution reacted in the outer layer of SMA-ECC, which is consistent with the conclusions of 4.1 and 4.2. In addition, the chloride ion concentration of SMA-ECC almost vanished at an erosion depth of 10 mm, which also corresponded to the results of the $AgNO_3$ solution color-rendering test of 4.3.

4.5. The Relationship between Apparent Chloride Ions Content and Time

Knowing the relationship between the chloride ion content and the erosion depth of SMA-ECC concrete under repeated dry-wet corrosion cycle, it can be found that the SMA-ECC specimen had the highest chloride ion content at the erosion depth of 0~5 mm, which can better characterize the relationship between the chloride ions content and corrosion age, and determine boundary conditions of the chloride ions content. A dry-wet cycle of four days was already mentioned. For more precise data, the corrosion age was converted to dry-wet cycle periods, e.g., 20 days were converted to 5 dry-wet cycles, and so on. Therefore, this paper performed linear regression on the chloride ion content and corrosion age at the surface of SMA-ECC specimen under dry-wet corrosion cycle. Using the Origin software, the relationship between the maximum chloride ion content on the surface of SMA-ECC specimen and corrosion age were fitted by exponential function, linear function, power function and logarithmic function, respectively [28,29]. The fitting curve of apparent chloride ion content of SMA-ECC specimens and time is shown in Figure 14.

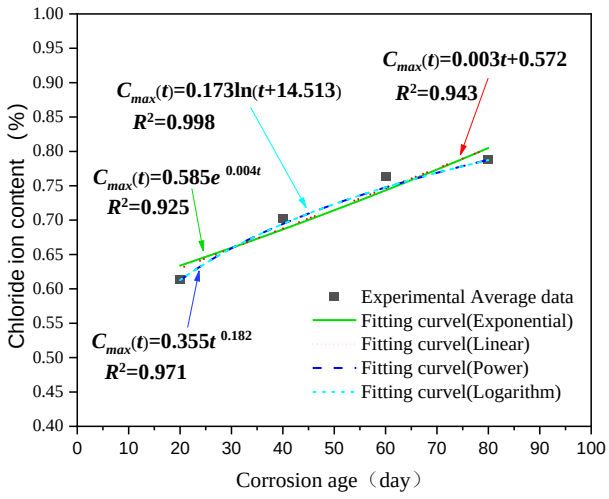


Figure 14. Fitting curve of apparent chloride ion content of SMA-ECC specimensand time.

It is clear from the above fitting curve that the exponential function, linear function, power function and logarithmic function correlation coefficient R^2 of SMA-ECC in the dry-wet cycle corrosion environment were 0.925, 0.943, 0.971 and 0.998, respectively. The larger the correlation coefficient R^2 were, the better the fitting effect of the function was, but the fitting situation of the function from the Origin needed to be considered [18]. Therefore, a power function model was used to characterize the law of surface chloride ion content and corrosion age of SMA-ECC in a dry-wet corrosion cycle environment, as shown in Formula (4), which showed that the power function can effectively fit the relationship between apparent chloride ion content and time [30]:

$$C_{max}(t) = 0.355t^{0.182} (R^2 = 0.971) \quad (4)$$

where $C_{max}(t)$ represents the maximum chloride ion content (%) on the surface of the specimen; t represents the corrosion age (day).

4.6. Apparent Chloride Ion Diffusion Coefficient of Equivalent Chloride Ion

The chloride ion erosion direction of the corroded specimen in the chloride salt dry-wet corrosion cycle environment was one-dimensional, and the apparent chloride ion diffusion coefficient can be calculated by Fick's second law [17]. The calculation Formula (5) is as follow:

$$C(x,t) = C_s \cdot \left[1 - erf\left(x/2\sqrt{Dt}\right)\right] \quad (5)$$

where $C(0,t) = Cs$ represents the diffusion boundary condition of chloride ions (%), taking 5%; $C(x,t)$ represents the chloride ion content (%); t represents the erosion time (s); x represents the erosion depth (m); D represents the chloride ion diffusion coefficient (m^2/s); $erf(x)$ represents the error function.

First, the implicit function solver of Fick's second law was programmed through MATLAB; Then, according to the test results and that the chloride ion content of the uncorroded specimen was about 0.007%, only instantaneous chloride ion diffusion coefficient D_{ins} of SMA-ECC within the erosion depth of 20 mm were calculated. The paper took the average value of D_{ins} under the same corrosion age, and performed nonlinear curve fitting of the relationship between D_{ins} and t, as shown in Figure 15.

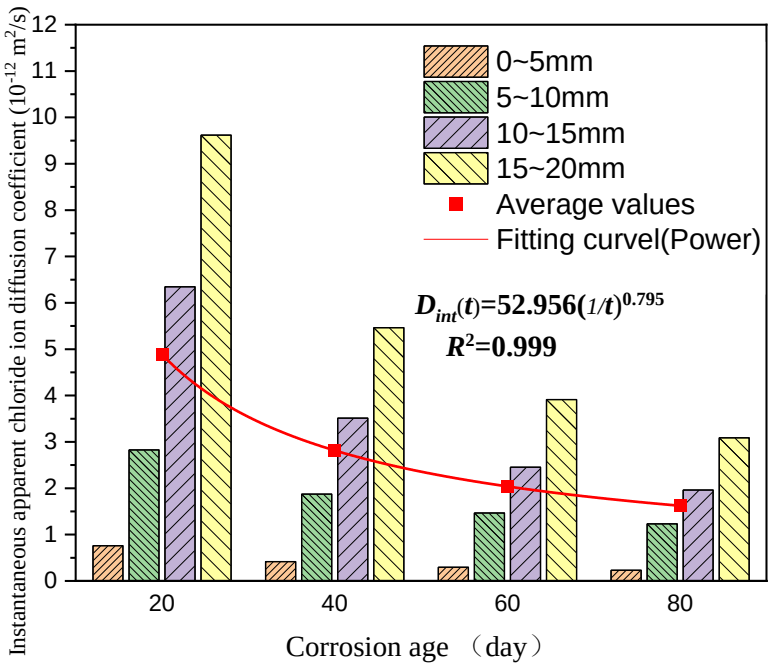


Figure 15. Instantaneous chloride ion diffusion coefficient D_{ins} of SMA-ECC.

The instantaneous apparent chloride ion diffusion coefficient of SMA-ECC was obtained by fitting the chloride ion distribution during the corrosion period. This coefficient cannot be regarded as the real diffusion coefficient at any time, but can be regarded as the integral value of the change of the diffusion coefficient during corrosion process [31]. The relationship between the apparent diffusion coefficient and the instantaneous diffusion coefficient of SMA-ECC is shown in Formula (6):

$$D_{app}(t) = \frac{\int_{t_0}^{t} D_{ins}(t)dt}{t - t_0} \tag{6}$$

where $D_{app}(t)$ represents the average value of the instantaneous diffusion coefficient of SMA-ECC from t_0 to t, namely the apparent diffusion coefficient of SMA-ECC (10^{-12} m^2/s); $D_{ins}(t)$ represents the average value of the instantaneous diffusion coefficient at time t (10^{-12} m^2/s).

From the relationship between the instantaneous chloride ion diffusion coefficient and time and the relationship between the apparent diffusion coefficient and the instantaneous chloride ion diffusion coefficient, the equivalent apparent chloride ion diffusion coefficient $D_{app}(t)$ in the dry-wet corrosion cycle, as shown in Formula (7):

$$D_{app}(t) = \left[\int_{t_0}^{t} 52.956 \times (1/t)^{0.795} dt\right] / (t - t_0) \tag{7}$$

where $D_{app}(t)$ represents the equivalent apparent chloride ion diffusion coefficient of SMA-ECC (10^{-12} m^2/s); t represents the corrosion age (day); t_0 represents the reference time point (day).

5. Conclusions

The chloride ion corrosion of SMA-ECC specimens under different times of dry-wet cycle was studied, compared with MC and ECC specimens in the same state. The chloride ion corrosion resistance was analyzed by the change of the mass of the specimen, the chloride ion transmission amount, the erosion depth and the chloride ion content after different times of dry-wet corrosion cycle. The major conclusions are as follows:

1. Compared with MC specimens, the mass change and chloride ion transmission of SMA-ECC were significantly larger than those of MC under the same corrosion condition, but the chloride ion erosion depth of SMA-ECC was obviously smaller than that of MC. These results showed that SMA-ECC undergoes more severe physical and chemical reactions during corrosion process and can better prevent chloride ions from eroding deeper places.
2. Although the chloride ion content of SMA-ECC was larger than that of MC at the same depth less than about 5 mm, the chloride ion content of SMA-ECC became shorter than that of MC at the depth more than about 5 mm. In addition, the chloride ion content of SMA-ECC was almost close to 0 at the erosion depth more than 10 mm, which was consistent with the test result of $AgNO_3$ solution color-rendering test and agreed with the analysis of results of Change law of corrosion depth of chloride ion.
3. Based on the erosion distribution of chloride ions and Fick's second law, Origin and Matlab software were used to solve and fit the calculation model of the apparent chloride ion diffusion coefficient and the boundary condition of the chloride ion content on the surface of SMA-ECC under dry-wet corrosion cycles, it was found that the power function has a good fitting effect.

Author Contributions: W.C.: Investigation, Methodology, Writing-original draft, Writing-review & editing. Y.L.: Formal analysis, Data curation, Writing-original draft, Software. H.Q.: Conceptualization, Methodology, Writing-review & editing, Supervision, Funding acquisition. P.W.: Investigation, Data curation, Writing-review & editing. Y.W.: Investigation. F.L.: Data analysis. All authors have read and agreed to the published version of the manuscript.

Funding: The research project reported in this paper was supported by a grant from National Natural Science Foundation of China (NSFC) through Grant No.51978631, Natural Science Foundation of Fujian Province No.2022J01557; Key Projects of Fujian Provincial Department of Transportation No.201914 and the Support Program for Innovative Research Team (in Science and Technology) in University of Henan Province (No. 23IRTSTHN006).

Data Availability Statement: All data, models, or code that support the findings of this study are available from the corresponding author upon reasonable request.

Conflicts of Interest: The authors declare no conflict of interest.

References

1. Tumidajski, P.; Chan, G. Durability of high performance concrete in magnesium brine. *Cem. Concr. Res.* **1996**, *26*, 557–565. [CrossRef]
2. Santamaría, A.; Orbe, A.; José, J.S.; González, J. A study on the durability of structural concrete incorporating electric steelmaking slags. *Constr. Build. Mater.* **2018**, *161*, 94–111. [CrossRef]
3. Aguirre, A.; de Gutiérrez, R.M. Durability of reinforced concrete exposed to aggressive conditions. *Mater. Constr.* **2013**, *63*, 7–38.
4. Seneviratne, A.; Sergi, G.; Page, C. Performance characteristics of surface coatings applied to concrete for control of reinforcement corrosion. *Constr. Build. Mater.* **2000**, *14*, 55–59. [CrossRef]
5. Zacharopoulou, A.; Zacharopoulou, E.; Batis, G. Protection systems for reinforced concrete with corrosion inhibitors. *Open J. Met.* **2014**, *4*, 86–92. [CrossRef]
6. Zafeiropoulou, T.; Rakanta, E.; Batis, G. Carbonation resistance and anticorrosive properties of organic coatings for concrete structures. *J. Surf. Eng. Mater. Adv. Technol.* **2013**, *3*, 67–74. [CrossRef]
7. Vyrides, I.; Rakanta, E.; Zafeiropoulou, T.; Batis, G. Efficiency of amino alcohols as corrosion inhibitors in reinforced concrete. *Open J. Civ. Eng.* **2013**, *3*, 33039. [CrossRef]
8. Li, R.; Hou, P.; Xie, N.; Ye, Z.; Cheng, X.; Shah, S.P. Design of SiO2/PMHS hybrid nanocomposite for surface treatment of cement-based materials. *Cem. Concr. Compos.* **2018**, *87*, 89–97. [CrossRef]
9. Thompson, J.L.; Silsbee, M.R.; Gill, P.M.; Scheetz, B.E. Characterization of silicate sealers on concrete. *Cem. Concr. Res.* **1997**, *27*, 1561–1567. [CrossRef]
10. Chousidis, N.; Ioannou, I.; Rakanta, E.; Koutsodontis, C.; Batis, G. Effect of fly ash chemical composition on the reinforcement corrosion, thermal diffusion and strength of blended cement concretes. *Constr. Build. Mater.* **2016**, *126*, 86–97. [CrossRef]
11. Fajardo, G.; Escadeillas, G.; Arliguie, G. Electrochemical chloride extraction (ECE) from steel-reinforced concrete specimens contaminated by "artificial" seawater. *Corros. Sci.* **2006**, *48*, 110–125. [CrossRef]
12. Carmona, J.; Garcés, P.; Climent, M. Efficiency of a conductive cement-based anodic system for the application of cathodic protection, cathodic prevention and electrochemical chloride extraction to control corrosion in reinforced concrete structures. *Corros. Sci.* **2015**, *96*, 102–111. [CrossRef]
13. Song, G.; Ma, N.; Li, H. Applications of shape memory alloys in civil structures. *Eng. Struct.* **2006**, *28*, 1266–1274. [CrossRef]
14. Maalej, M.; Hashida, T.; Li, V. Effect of fiber volume fraction on the off-crackplane fracture energy in strain-hardening engineered cementitious composites. *J. Am. Ceram. Soc.* **1995**, *78*, 3369–3375. [CrossRef]
15. Chen, W.; Feng, K.; Wang, Y.; Lin, Y.; Qian, H. Evaluation of self-healing performance of a smart composite material (SMA-ECC). *Constr. Build. Mater.* **2021**, *290*, 123216. [CrossRef]
16. Chen, W.; Lin, B.; Feng, K.; Cui, S.; Zhang, D. Effect of shape memory alloy fiber content and preloading level on the self-healing properties of smart cementitious composite (SMA-ECC). *Constr. Build. Mater.* **2022**, *341*, 127797. [CrossRef]
17. Sun, R.; Hu, X.; Ling, Y.; Zuo, Z.; Zhuang, P.; Wang, F. Chloride diffusion behavior of engineered cementitious composite under dry-wet cycles. *Constr. Build. Mater.* **2020**, *260*, 119943. [CrossRef]
18. Huang, D.; Niu, D.; Su, L.; Fu, Q. Chloride diffusion behavior of coral aggregate concrete under drying-wetting cycles. *Constr. Build. Mater.* **2020**, *270*, 121485. [CrossRef]
19. Huang, D.; Niu, D.; Zheng, H.; Su, L.; Luo, D.; Fu, Q. Study on chloride transport performance of eco-friendly coral aggregate concrete in marine environment. *Constr. Build. Mater.* **2020**, *258*, 120272. [CrossRef]
20. Yang, Y.; Lepech, M.D.; Yang, E.H.; Li, V.C. Autogenous healing of engineered cementitious composites under wet–dry cycles. *Cem. Concr. Res.* **2009**, *39*, 382–390. [CrossRef]
21. Alyousif, A.; Lachemi, M.; Yildirim, G. Effect of Self-Healing on the Different Transport Properties of Cementitious Composites. *J. Adv. Concr. Technol.* **2015**, *13*, 112–123. [CrossRef]

22. Moon, G.D.; Oh, S.; Choi, Y.C. Effects of the physicochemical properties of fly ash on the compressive strength of high-volume fly ash mortar. *Constr. Build. Mater.* **2016**, *124*, 1072–1080. [CrossRef]
23. Ye, H.; Jin, X.; Fu, C.; Jin, N.; Xu, Y.; Huang, T. Chloride penetration in concrete exposed to cyclic drying-wetting and carbonation. *Constr. Build. Mater.* **2016**, *112*, 457–463. [CrossRef]
24. Shi, C.; Hu, X.; Wang, X.; Wu, Z.; Schutter, G.D. Effects of Chloride Ion Binding on Microstructure of Cement Pastes. *J. Mater. Civ. Eng.* **2017**, *29*, 4016181–4016183. [CrossRef]
25. Thoft-Christensen, P. Deterioration of Concrete Structures. In Proceedings of the First International Conference on Bridge Maintenance, Safety and Management, LABMAS, Barcelona, Spain, 14–17 July 2002.
26. Ehlert, R. Coral concrete at Bikini Atoll. *Concr. Int.* **1991**, *13*, 19–24.
27. Hua, Y.; Yin, Y.P.; Yu, Y.L.; Li, S. Research on chloride diffusion and flexural behavior of beams strengthened with TRC subjected to dry-wet cycles. *Constr. Build. Mater.* **2019**, *229*, 116906.
28. Yang, L.; Cai, R.; Yu, B. Investigation of computational model for surface chloride concentration of concrete in marine atmosphere zone. *Ocean Eng.* **2017**, *138*, 105–111. [CrossRef]
29. Pack, S.W.; Jung, M.S.; Song, H.W.; Kim, S.H.; Ann, K.Y. Prediction of time dependent chloride transport in concrete structures exposed to a marine environment. *Cem. Concr. Res.* **2010**, *40*, 302–312. [CrossRef]
30. Özbay, E.; Šahmaran, M.; Lachemi, M.; Yücel, H.E. Self-healing of microcracks in high-volume fly-ash-incorporated engineered cementitious composites. *ACI Mater. J.* **2013**, *110*, 33–43.
31. Van den Heede, P.; De Keersmaecker, M.; Elia, A.; Adriaens, A.; De Belie, N. Service life and global warming potential of chloride exposed concrete with high volumes of fly ash. *Cem. Concr. Compos.* **2017**, *80*, 210–223. [CrossRef]

Disclaimer/Publisher's Note: The statements, opinions and data contained in all publications are solely those of the individual author(s) and contributor(s) and not of MDPI and/or the editor(s). MDPI and/or the editor(s) disclaim responsibility for any injury to people or property resulting from any ideas, methods, instructions or products referred to in the content.